Abridgment of nano and micro length scale mechanical properties of novel Mg–9Li–7Al–1Sn and Mg–9Li–5Al–3Sn–1Zn alloys using object oriented finite element modeling

Ankur Gupta [a,b], Vinod Kumar [a,c], Jitin Nair [d], Ankit Bansal [a,e], Kantesh Balani [a,*]

[a] Department of Materials Science and Engineering, Indian Institute of Technology, Kanpur 208016, India
[b] Advanced Materials Processing and Analysis Center, Department of Materials Science and Engineering, University of Central Florida, Orlando, FL 32826, USA
[c] Department of Metallurgical and Materials Engineering, Malaviya National Institute of Technology, Jaipur 302017, India
[d] Department of Materials and Metallurgical Engineering, National Institute of Foundry and Forge Technology, Ranchi 834003, India
[e] Tata Steel Ltd., Jamshedpur, Jharkhand 831001, India

ABSTRACT

In the recent years, magnesium–lithium (Mg–Li) alloys have attracted considerable attention/interest due to their high strength-to-density ratio and damping characteristic; and have found potential use in structural and biomedical applications. Here the mechanical behavior of novel Mg–9 wt.% Li–7 wt.% Al–1 wt.% Sn (LAT971) and Mg–9 wt.% Li–5 wt.% Al–3 wt.% Sn–1 wt.% Zn (LATZ9531) alloys is reported. Both, as cast and thermomechanically processed alloys have been studied which possess dual phase microstructure. Nanoindentation data have been utilized to envisage the elastic modulus of alloy via various micromechanics models (such as rule of mixtures, Voigt–Reuss, Cox model, Halpin–Tsai and Guth model) in order to estimate the elastic modulus. Object oriented finite element modeling (FEM) has been performed to predict stress distribution under tensile and compressive strain state. Close match between Halpin–Tsai model and FEM results show the abridgment of nano length scale property to evolution of microscopic stress distribution in novel LAT971 and LATZ9531 Mg–Li–Al based alloys.

© 2015 Elsevier B.V. All rights reserved.

1. Introduction

High strength-to-density ratio (158 kN m/kg) and high elastic modulus-to-density ratio (25.89 MPa/kg m^{-3}), damping behavior and excellent electromagnetic shielding of magnesium (Mg) make it an ideal materials for light weight structural applications [1,2]. However, processing of Mg is always difficult due to its hexagonal closed packed (HCP) crystal structure. Low density lithium (Li) is usually added as alloying element in Mg to overcome this short-coming and further reduces its density [3]. According to the Mg–Li binary phase diagram, body centered cubic (BCC) β-phase of Li solid solution co-exist with HCP α-phase of Mg solid solution in the range of 5–11 wt.% Li [3–5]. However, Mg–Li alloys do not develop sufficient strength for structural use. Chang et al. [6] have reported that addition of 1 wt.% Zn in Mg–9Li alloy enhances the tensile strength by 41.8 MPa at the expense of elongation by 25%. This strengthening of Mg–Li alloys is attributed to the dissolution of Zn in α-Mg solid solution phases by solid solution strengthening

[2]. Moreover, poor corrosion resistance of Mg also inhibits a wider application of Mg alloys [7]. It has been reported in the literature that addition of aluminum (Al) into the Mg matrix not only provide corrosion resistance, it also contributes significantly to improve the strength of the alloy [8,9]. As a result of the above, complex microstructures have been observed in Mg–Li based alloys which make it difficult to estimate the mechanical properties of the processed alloys [10,11]. Low stiffness of metallic structural component such as Mg–Li based alloys also limit its use in high performance automotive and aerospace applications as they deform under loading [12]. Therefore, high stiffness of structural material is always prime concern for design engineers. As a result of this, behavior of metallic materials under loading conditions have always a great interest to material scientists. Design engineers have been analyzing the stress distribution and elastic property of the component subjected to loading and others parameters to simulate the real world condition utilizing Pro/Engineer®, COM-SOL®, SolidWorks® software packages. Despite their efforts, failure of component still possesses uncertainty over life time and material performance due to the lack of understanding of material's response to different stress conditions. It is well known that crystal

structure, nature of grain boundaries (such as high angle, low angle and twin), shape and size of precipitates, mechanical properties, etc. of the material influence the formability process and mechanical performance while subjected to field applications. Thus, it becomes necessary to understand the influence of microstructure (incorporating precipitates shape and size; grain boundaries) and mechanical properties of intended material. Most of the models, developed for mechanical properties estimation, take care of volume fraction and shape of the second phase or pores by assuming these to be spherical, elliptical or rod like, etc. [13–15]. However in actual situations, irregular shape of pores and second phase are responsible for unpredictable results [13]. Thermomechanical processing of cast alloys break the segregation of precipitates and reduce the grain size and shape in case of recrystallization. Kumar et al. [11] have reported that thermomechanical processing of cast Mg–Li alloy also resulted in interesting texture evolution. Texture analysis of these Mg–Li alloys in cast and rolled condition shows an increased activity of non-basal $(1\,0\,\bar{1}\,0)$ slip plane. Electron backscattered diffraction (EBSD) analysis of cast and rolled Mg–Li alloys also indicates the presence of strain free grains and average grain misorientation of <2° in thermomechanically processed alloy. Therefore, mechanical response of cast and thermomechanically processed alloys will vary under different loading conditions.

Object oriented finite element modeling (OOFEM) is an effective technique to study the complexity of microstructure in terms of grains, grain boundaries, second phase, pores, etc. to predict mechanical and thermal properties; and stress analysis because FEM has the advantage of readily incorporating microstructural details of various phases [16]. Microscopic images are utilized to construct the skeleton, and the fundamental properties the finite element mesh are assigned (such as elastic modulus, Poisson's ratio, or thermal conductivity) belonging to each constituting phase. As a result, a specific property of material, as a whole, can be estimated, viz. estimating elastic modulus of turtle's complex carapace [17], thermal conductivity of Al–Si–CNT composites at various length scales [18], effective elastic modulus of Ni–Al$_2$O$_3$ interpenetrating composites [19], etc.

This paper incorporates utilizing various micromechanics models (such as rule of mixtures, Voigt–Reuss, Cox model, Halpin–Tsai and Guth model) in order to estimate the elastic modulus. Using OOFEM, Mg–Li based alloys have been analyzed in both: (i) as cast, and (ii) thermomechanically processed conditions as a response to various strain states within elastic limits. The predicted values of effective elastic modulus (obtained from OOFEM) have been compared with established micromechanics models. Further, the stress distribution and effective elastic modulus of novel Mg–9Li–7Al–1Sn (LAT971) and Mg–9Li–5Al–3Sn–1Zn (LATZ9531) alloys are developed using OOFEM, in order to observe the stress-concentration (during application of strain) resulting due to complexity of microstructure.

2. Material processing

LAT971 and LATZ9531 alloys were cast in an induction furnace and thermomechanically (TM) processed (hot-rolled at 573 K) as reported in earlier publications [10,11,20]. These TM processed samples of LAT971 and LATZ9531 have been denoted as LAT971R and LATZ9531R, respectively. The microstructure of the as cast and TM processed alloys were observed in scanning electron microscope (SEM, ZEISS EVO 50) equipped EDS facility utilizing backscattered mode to get good atomic number contrast to identify different phases and precipitates present in the processed alloys. Elastic modulus of each phase present in the as cast and TM processed alloys was obtained via nanoindentation (Hysitron Inc., Minneapolis, MN, USA) with Berkovich pyramidal tip of ~100 nm [10,20] using Oliver and Pharr method [21].

2.1. Microstructural and compositional analysis

X-ray diffraction and electron probe micro-analyzer (EPMA) techniques were utilized to identify phases and their respective composition present in the alloy [11]. LAT971 and LATZ9531 have dual phase (α- and β-) microstructure, detailed and labeled micrographs of which (both cast and rolled LAT971 and LATZ9531 alloys) have been presented in Fig. 1(a)–(d). The α-phase was found to be Mg rich possessing HCP structure, while, the β-phase was rich in Li possessing BCC structure. Two types of precipitates were also observed in both the alloys in cast as well as rolled condition. Brighter precipitates embedded in α-phase were found to be Mg-Li-Sn rich composition as observed by EPMA and precipitates embedded in β-phase were Mg-Al-Li rich with composition MgLi$_2$Al [11]. Therefore, each microstructure (cast and rolled) was observed to be consisting of four different phases.
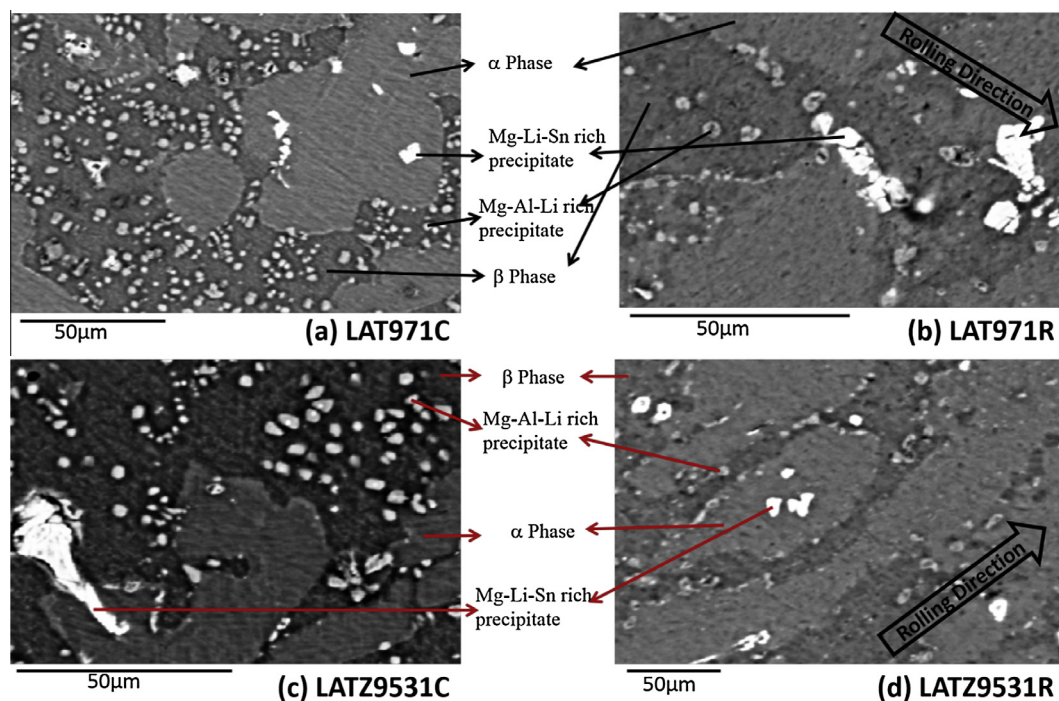
Fig. 1. Back scattered SEM micrographs of (a) as cast LAT971, (b) rolled LAT971, (c) as cast LATZ9531 and (d) rolled LATZ9531 alloys showing dual phase microstructure and precipitates.

Table 1
Elastic modulus (*E*) and Poisson's ratio (υ) values assigned to different phases in finite element OOF2 modeling.

Phase	LAT971C		LAT971R		LATZ9531C		LATZ9531R	
	E (GPa)	υ	*E* (GPa)	Y	*E* (GPa)	υ	*E* (GPa)	υ
Alpha	58.5	0.291	58.8	0.291	58.8	0.291	60.5	0.291
Beta	63.4	0.362	59.6	0.362	61.2	0.362	51.0	0.362
Mg–Li–Sn rich ppt in alpha	6.30	0.361	15.3	0.361	7.70	0.361	14.6	0.361
Mg–Al–Li rich ppt in beta	15.6	0.340	20.7	0.340	34.0	0.340	19.2	0.340

2.2. Computational methods

2.2.1. Mesh creation, material property assign and refinement

Back scattered electron images of these alloys were used for stress analysis and effective elastic modulus estimation using OOF2 software package. For analysis, each phase was assigned a pixel group by rigorous pixel selection techniques followed by assigning materials to each pixel group and at last assigning different elastic properties (elastic modulus and Poisson's ratio) to each phase. Elastic modulus (*E*) of alpha and beta phases as well as precipitates were obtained from nanoindentation test [20]. Poisson's ratio of each phases was assumed to be equal to major element in the corresponding phase based on EPMA results [10] and was assigned to the corresponding pixel group. Table 1 summarizes the elastic modulus and Poisson's ratio assigned to different phases of Mg–Li based alloys for OOFEM models.

An image identical to the microstructure of alloy was formed after assigning material properties and color to the pixels belonging to different phases and was used to create the skeleton. The mesh of pixel group boundary was constructed by using different adaptive mesh refining techniques. The discretization of image was facilitated by adaptive mesh option such that pixel boundary is confined by: (i) homogeneity and (ii) shape of the element [17]. The shape energy (*E_{shape}*) is a measure of feature of the shape of elements, and the homogeneity energy (*E_{hom}*) defines the quality of adaption of the mesh with the pixel regions [22]. Some of the mesh adjustment practices move the mash nodes by assuming them as particles which associate the shape and homogeneity function, hence the term energy are frequently used to define them [16]. These two factors can be combined by a tunable parameter α through Eq. (1) [22]:

$$E_{element} = \alpha \cdot E_{hom} + (1 - \alpha) \cdot E_{shape} \qquad (1)$$

where α varies between 0 and 1. *E_{element}* is effective element energy. *E_{hom}* and *E_{shape}* are the functions that depend on the homogeneity and shape of the elements [16]. The refine tool was used to chop bigger elements at the boundary and convert them into smaller pieces followed by moving the element nodes at the pixel boundaries by a snap tool. Bad shape elements were avoided by intermediate rationalization tools. Smooth and anneal tools were utilized to move the nodes according to the selected criterion. Fix illegal elements tool was used to remove the illegal elements in the mesh [16]. The actual boundary of the mesh was obtained by intense refinement of pixels at the boundary. This has resulted in the finite element meshes with the attributes listed in Table 2. The homogeneity index >0.95 was targeted and achieved in all the cases.

2.2.2. Boundary conditions

After constructing the mesh, the boundary condition was chosen to a fixed strain to avoid the structure movement while applying the strain and simultaneously the deformation can be captured. Top and bottom boundaries were constricted adiabatically i.e. σ = 0 (zero stress). The left boundary was kept fixed and the tensile and compressive strain was applied on the right boundary. The OOF2 software package utilize conventional force balance equation to solve the finite element meshes for different properties by conjugate gradient method [23].

$$\nabla \cdot \sigma = f \qquad (2)$$

$$\sigma = \sum k \nabla \varphi \qquad (3)$$

where, σ, *f*, φ, and *k* are flux, applied force, displacement and coupling constant. Strain in the range of 0.24–6.18% was selected based on the HCP crystal structure possessing limited slip systems in Mg and because most of the components fail within their elastic limit. Secondly, the objective of this study is to capture the regions of

Table 2
Mesh attributes for finite element mesh constructed for as cast and rolled LAT971 and LATZ9531 alloys.

Specimen	Nodes	Elements	Triangles	Quadrilaterals	Homogeneity
LAT971C	12,121	18,946	14,033	4913	0.95546
LAT971R	8631	13,421	9895	3526	0.96467
LATZ9531C	7363	11,590	8715	2875	0.95176
LATZ9531R	3559	5632	4343	1289	0.95997

stress-concentrations responsible for structural failure during service period of the component. The effective elastic modulus of the alloys was calculated from the integrated stress at the right side boundary for all the cases.

3. Results and discussion

3.1. Estimation of effective elastic modulus of Mg–Li alloys

Mechanical properties of the Mg–Li based LAT971 and LATZ9531 alloys in cast and rolled condition have been estimated using various micromechanical models (rule of mixtures, Voigt–Reuss, Cox model, Halpin–Tsai and Guth model). As mentioned earlier, LAT971 and LATZ9531 alloys have dual phase microstructure and each phase contains precipitates. It is also clear from Fig. 1 that the α- and β-phase grains are randomly oriented. Microstructure also show the nature of precipitates such as segregation, irregular shape, presence at/or near the grain boundary further adding complexity in the microstructure. These factors, individually or combined, influence the mechanical properties, therefore must be taken care of while selecting the material. On the other hand, each micromechanics models have been developed considering intrinsic and extrinsic factors/assumptions such as the volume fraction, distribution of reinforcement/inclusion and applied load, relative distribution of applied load/stress/strain, porosity; aspect ratio of reinforcement phase and so on and has their own limitations. Therefore, it is difficult to select one micromechanics model based on microstructure visualization as assumptions of several models have overlap among different phases of the microstructure. Therefore, several micromechanics models have been utilized to compare their finding with FEM results and find out the suitable micromechanics model for novel Mg–Li alloys. However, elastic modulus of alloys can be measured using nanoindentation technique. But measurement of elastic modulus from nanoindentation method on 100 μm × 100 μm area of sample is very time consuming process and nanoindentation instrument may not be easily assessable. In the light of these facts, finding suitable micromechanics model will provide an additional and quick method to estimate the mechanical properties of metallic alloys. On the other hand, these micromechanics models are widely used in software programs developed for materials analysis. Therefore, this study is a synergistic approach in comparing available mechanics model and finite element modeling software.

These models have been developed for polymer matrix composites, but have been applied to metal matrix and ceramic matrix composites as well [18,24–27]. Usually, conventional composite materials have stiffer reinforcement phase than matrix. The function of the matrix is to transfer the applied load to the reinforcement phase while reinforcement, but in the present case of Mg–Li based alloys, hardness and stiffness of precipitate is lower than that of α- and β-phase of Mg–Li alloys (see Table 1). The mathematical equation of different micromechanics models utilized in this present study can be found in Supplementary Information. All of these models expresses the effective elastic modulus of linearly elastic matrix with precipitates as reinforcement. Rule of mixture and combined Voigt–Reuss model does not depend on shape of

Table 3
Volume fraction of phases and precipitates observed in LAT971 and LATZ9531 alloy [10].

Sample	Volume fraction			
	α-phase	Mg–Li–Sn rich ppt in α-phase	β-phase	Mg–Al–Li rich ppt in β-phase
LAT971C	0.67	0.01	0.29	0.03
LAT971R	0.67	0.01	0.29	0.03
LATZ9531C	0.59	0.03	0.31	0.07
LATZ9531R	0.59	0.03	0.31	0.07

the precipitates, while Cox, Halpin–Tsai and Guth models include the effect of shape and size of precipitates on elastic modulus.

To estimate the elastic property, Mg–Li–Sn and Mg–Al–Li rich precipitates were considered as reinforcement in α- and β-phase, respectively and micromechanical models were applied to obtain the elastic property of α-region and β-region. Then, β-region was considered as the reinforcement and α-region as matrix due to their respective volume fraction (see Table 3). Again, micromechanics models were applied to obtain the overall elastic property of composite microstructure. Elastic modulus of α-, β-, Mg–Li–Sn rich and Mg–Al–Li rich precipitates measured from nanoindentation were utilized to estimate the effective elastic modulus of the alloys [20]. Relative volume fraction of matrix and precipitate phases were analyzed from microstructure analysis software (imageJ) and are listed in Table 3. Authors have assumed here that thermomechanical treatment does not change the relative volume fraction of matrix and precipitates phases, therefore, volume fraction in the as cast and rolled condition remains the same. The volume fraction of the second phase (β-phase and Mg–Al–Li precipitates) is in the range of 0.32–0.38, hence the system is considered to be dilute (except for Guth model as explained later) since Mg–Li based alloys systems satisfy the assumptions of these micromechanics models. Aspect ratio of precipitates, α- and β-phase was calculated from microstructure measured using an

average of five micrographs. Calculated results of effective elastic modulus from models have been summarized in Table 4.

Effective elastic modulus of Mg–Li based alloys was also calculated from FEM method. Different strains were applied on the constructed mesh of each alloy (LAT971 and LATZ9531; as cast and rolled) in terms of pixel displacement and stresses were captured as cumulative stress average of each pixel. The loading condition was specified in OOF2 in terms of displacement of boundary. In all cases, the boundary was displaced by 1, 5, 11, 20 and 25 pixel units. The average length of the micrograph used for OOF2 modeling was 405 pixels. Therefore, the applied strain is equivalent to ~6%, the maximum strain for tensile and compressive loading condition. Stress corresponding to varying strain levels is shown in Fig. 2 and effective elastic modulus of alloys in both cast and rolled conditions are listed in Table 4.

It can be observed from Table 4 that the effective elastic modulus obtained from FEM modeling possess slightly lower values than the α- and β-phase those measured by nanoindentation (Table 1), which may be attributed to the low elastic modulus of precipitate phase. Furthermore, lower effective elastic modulus than the α- and β-phase can be reasoned to the dissolution of other alloying elements in the α- and β-phase and precipitates [11]. As mentioned above, while assigning the properties to the color coded replica of micrograph, the Poisson's ratios were assumed based on the highest concentration of element presented in the individual phase. Since the modulus of different phases were taken from nanoindentation data, assumption of Poisson's ratio can change in the applied strain on the mesh and result in the slightly lower values of effective elastic modulus of alloys.

Despite the similar stress contours and elastic properties, average strain in case of rolled LATZ9531 alloy has been observed to be higher than rest of the alloys. The number of mesh attributes for alloy LATZ9531R is less (~14,500) whereas in all other cases it is in range of 30,000–50,000 (see Table 2). Since, the displacement conditions were kept same across all samples, the average strain for individual elements/attributes will be higher when number of

Table 4
Comparison of effective elastic modulus (GPa) estimated from different models.

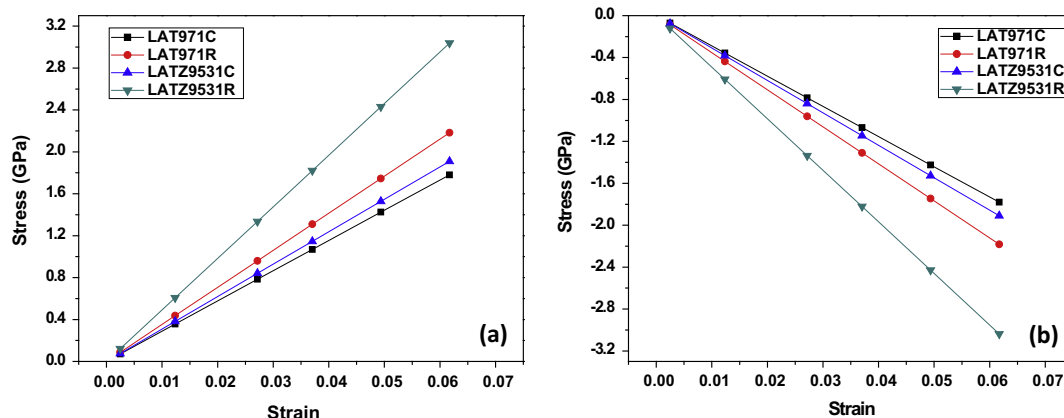| Sample	Rule of mixture (GPa)		Combined Voigt–Reuss method (GPa)	Cox method (GPa)	Halpin–Tsai method (GPa)	Guth method (GPa)	Finite element OOF2 modeling (GPa)
	Lower limit	Upper limit					
LAT971C	51.2	58.1	55.5	42.8	57.5	127.1	55.1
LAT971R	54.5	57.5	56.3	42.9	57.1	384.5	60.6
LATZ9531C	47.5	56.3	53.0	38.5	55.6	188.1	53.6
LATZ9531R	46.4	53.3	50.7	39.0	52.4	426.2	60.1

Fig. 2. Variation of stress with changing boundary displacement for LAT971 and LAT9531 alloys in as cast and rolled conditions: (a) tensile and (b) compressive strain.
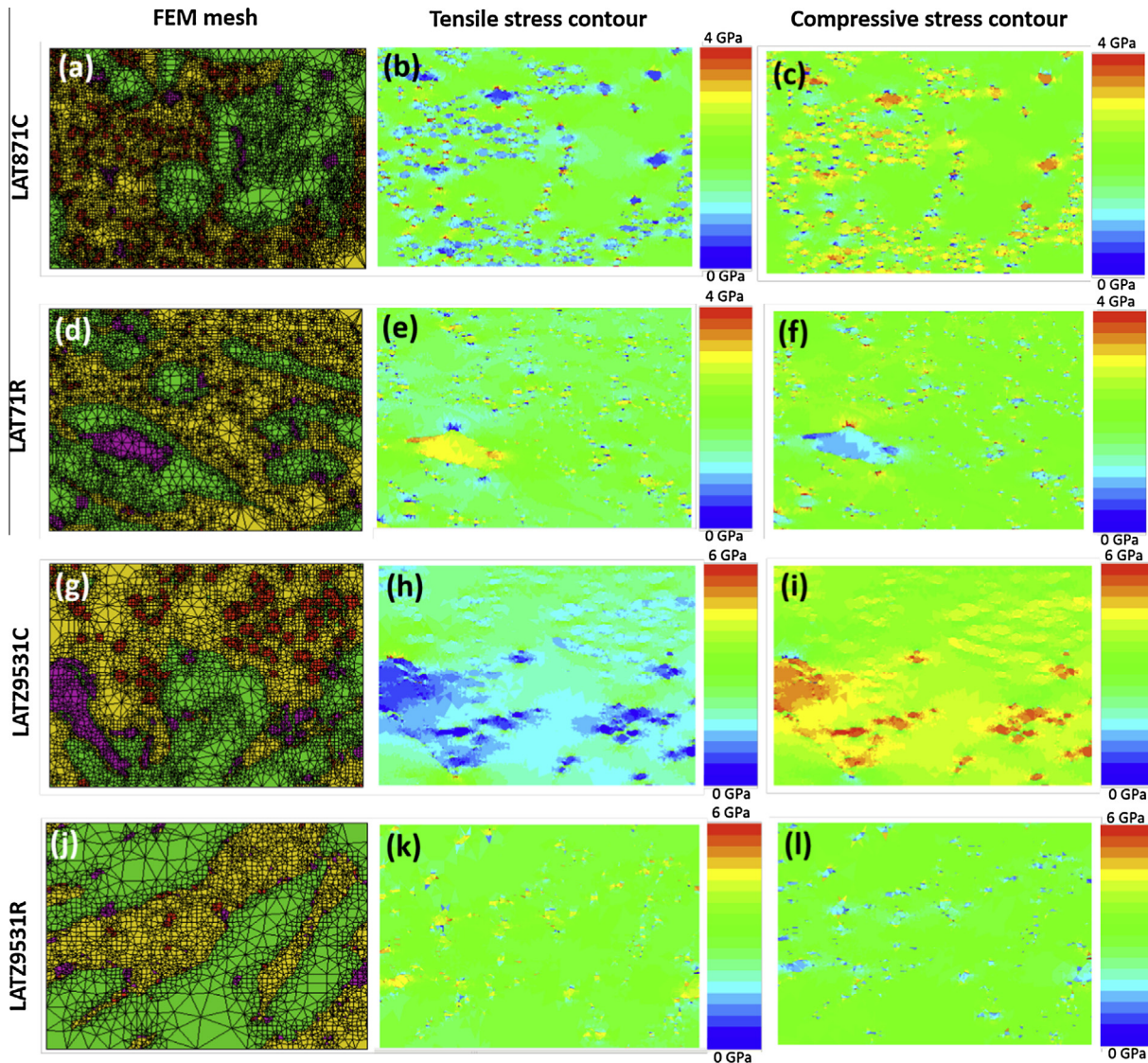
Fig. 3. Two dimensional FEM stress analysis from micrograph: (a), (d), (g) and (h) finite element mesh applied on color coded replica of micrograph presented in Fig. 1 where four different color depicts different phases in LAT971 and LATZ9531 alloys in as cast and rolled condition. Tensile and compressive stress contour (shown on color scale) corresponding to the 6.18% strain applied on (b) and (c) LAT971C, (e) and (f) LAT971R, (h) and (i) LATZ9531C and (k) and (l) LATZ9531R alloys. (For interpretation of the references to colour in this figure legend, the reader is referred to the web version of this article.)

elements is less. On the other hand, it can be understood as the elements are of larger size i.e. lesser in number; there would be large continuous part in the microstructure. Homogenization treatment of cast alloys relieves the residual stress in the samples, whereas thermomechanical treatment might induce residual stresses in the alloys resulting in higher elastic modulus. Our previous research revealed that α-phase of rolled alloys contain an order of higher dislocation density than β-phase and pure Mg [20]. As a result of this, 16–22 pop-in-events were recorded in rolled α-phase compared to 10–15 in rolled β-phase of LAT971 and LATZ9531 alloys [20], which clearly signifies the role of thermomechanical treatment on mechanical properties of Mg–Li alloys.

The comparison of effective elastic modulus from FEM and micromechanics models indicate large variation in the estimated values. Guth model over predicts the modulus values of Mg–Li based alloys due to the high volume fraction of the second phase (β-phase and Al–Li precipitates). Guth model was originally developed for small amount of filler loading (⩽0.1 volume faction) in polymer matrix [28]. But, with increasing volume faction of filler or reinforcement phases, Guth models highly over predicts the

modulus values. Therefore, concentration of second phase is considered to be non-dilute for Guth model in Table 1 in Supplementary Information. This behavior of Guth model was also witnessed while calculating the elastic modulus of α-and β-region having Mg–Li–Sn rich and Mg–Al–Li rich inclusions. The volume fraction of these inclusions is <9 vol.% and estimated elastic modulus was in the range of 60–73GPa in different alloy conditions. These modulus values match closely when compared with other micromechanics models (Table 4).

Unlike the Guth model, Cox model under predicts the elastic modulus of alloys as it depends strongly on shape of the particle rather than volume fraction alone. In the present study, shape of the precipitates in the Mg–Li based alloys is irregular and gets precipitated form clusters and chains as clearly visible in Fig. 1. Precipitate-clusters and chains formed within the composites change the load bearing ability, which are not accounted by the micromechanical models. Additionally, reinforcing effect of precipitates occurs when the aspect ratio is higher than the critical value, which varies with the materials [29]. In the present study, the aspect ratio of Mg–Li–Sn rich precipitate was 3.5–4.5 whereas that for Mg–Al–Li

was 1.1–1.5. Therefore, this large variation in aspect ratio is also likely to cause the reduced estimated elastic modulus.

Elastic modulus estimated from Halpin–Tsai, rule of mixture (ROM) and combined Voigt–Reuss (CV–R) model resembles well with the results obtained from FEM. Yan et al. [29] have reported that particle type and shape has very little effect on elastic modulus for particulate reinforced polymer matrix composites estimated using Halpin–Tsai method and results shows excellent correlation with the experimental results. With increasing reinforcement volume fraction, elastic modulus is observed to increase when estimated from Halpin–Tsai, ROM and CV–R method. These models are applicable to wide range of volume fraction of reinforcement phase. Therefore, elastic modulus estimated from these models shows good correlation with the modulus obtained from FEM. This evinces that Halpin–Tsai model is highly accurate in estimating the mechanical property followed by CV–R and ROM.

3.2. Effect of microstructure on stress distribution in Mg–Li based alloys

Object oriented finite element analysis technique was utilized to generate the normal stress σ_y while loading under tensile and compressive state. Fig. 3 shows the simulated stress distribution in alloys developed when subjected to mechanical loading via FEM for as cast and rolled Mg–Li based LAT971 and LATZ9531 alloys. Fig. 3(a), (d), (g) and (j) are color coded replica of FEM mesh constructed from the micrograph by assigning materials to different pixel groups corresponding to different phases from OOF2 software package. Four different colors in each FEM mesh represent different phases and precipitates in LAT971 and LATZ9531 alloys. The mesh appears to be well homogenized and pixel boundaries are well confirming with element boundaries. Values of strain were selected by keeping HCP structure of Mg in mind. High strain leads to fracture during thermomechanical processing of Mg based alloys. Tensile and compressive stress contour (shown on color scale) corresponding to the 6.18% strain applied on each alloy have been shown for each alloy alongside of their corresponding FEM mesh in Fig. 3. Heterogeneous stress distribution have been observed in the cast and rolled alloy, which illustrates that the stress is concentrated in bulk α-phase in contrast to bulk β-phase due to the mismatch in the elastic modulus. The tensile stress varies between 0.2 and 3.8 GPa (Fig. 3(a) and (b)) and 0.2–3.4 GPa (Fig. 3(d) and (e)) in as cast and rolled LAT971 alloy, respectively, whereas for compressive strain condition, stress varies between 0.2 and 3.6 GPa (Fig. 3(c)) and 0.6–3.8 GPa (Fig. 3(f)) in as cast and rolled LAT971 alloy, respectively. The color coded scale bar along the stress contours has been calibrated in equal units with 20 such units. Hence each unit is corresponding to 0.2 GPa (in case of 0–4) and 0.3 GPa (in case of 0–6). Response of LATZ9531 alloy (Fig. 3(g) and (l)) in cast and rolled condition also depicts the behavior similar to LAT971 alloy as shown in Fig. 3. The compressive stress varies between 0.6 and 5.7 GPa in both (Fig. 3(i) and (l)), as cast and rolled LAT971 alloy. In some of the contour maps, a sudden increase in the compressive stress is evident in the form of spikes (see Fig. 3), which is attributed to either a few oddly shaped mesh elements or presence of fine precipitates. But, the tensile and compressive stress as high as 3.8 or 5.7 GPa, respectively, is observed in these simulations, which may not be experienced in service. In the current study, elastic modulus of different phases present in alloys was measured from nanoindentation and utilized for FEM study. It must be mentioned that elastic modulus obtained from nanoindentation are usually higher and exists at nano length scale. However, defects such as dislocation, twin boundaries, porosity and vacancy lower the elastic modulus at macroscopic scale. Similarly, stress may accordingly be rationalized at macroscopic scale in the current work.

The variation in the localized stress-concentration is ascribed to the microstructural heterogeneity of alloys. Ganesh et al. [30] have reported a generated stress of 675 MPa at triple junctions (diffusion barrier meeting two copper grain boundaries) in 120 nm copper interconnects upon thermal cycling, which has resulted in stress-induced void formation. As reported above, stress in the as cast and rolled microstructures has been found to be very similar, which is attributed to the repeated annealing between each pass during TM treatment at 573 K. However, it has been observed from stress contours that stress distribution is more homogeneous in rolled alloys in comparison to that of cast alloys. Breaking of the agglomerated precipitates during TM treatment could be the reason as it is clearly visible from the microstructure that precipitates are uniformly distributed and elongated in the rolling direction (Fig. 1).

It is also illustrated from stress contours that Mg–Al–Li rich precipitates embedded in the β phase act as stress relaxers. Most of the stress concentration was observed in the regions around Mg–Li–Sn rich precipitates in the α phase. Elastic modulus of Si rich precipitates is lower (6.3–7.7 GPa) than Al–Li rich precipitates (16.6–34 GPa) in cast conditions (see Table 1), therefore, stress is effectively transferred from precipitates to the surrounding matrix through interface.

However, in case of large mismatch between elastic modulus of precipitates and surrounding matrix, these interface sites act as stress concentrator. Agglomerated precipitated particle, precipitates with sharp edges, corners, notches and porosity; and precipitates near to grain boundary also behave as stress concentrator and/or relaxer especially for as cast alloys as evinced from the stress contours (Fig. 3). On the other hand, TM processing not only breaks the agglomerates of Al–Li precipitates but also distributes them uniformly in the β-phase (Fig. 1). As mentioned before, the strain of ~6% was chosen with the consideration of linear elastic behavior of Mg based metallic alloys. Therefore, a comparison of elastic properties of alloys obtained from micromechanical models can be made with FEM modeling results. Similarly, transformation induced plasticity (TRIP) and dual phase (DP) steel were analyzed from FEM method, and have shown that martensite phase bears large part of the stress transferred through ferrite phase in DP steel [31]. Whereas, in the case of TRIP steel, interaction between ferrite, martensite and austenite phases develops more complex stress distribution and deformation process [31]. Thus, processing and complexity of microstructure may lead to more sophisticated localized stress-concentration in the material and dictate the resulting mechanical behavior during service.

Fig. 4 shows a schematic representing the processing of as cast and rolled LAT971 and LATZ9531 alloys. The schematic also illustrates the effect of Mg–Li–Sn rich and Mg–Al–Li rich precipitate phases and their shape, distribution and respective volume. Bigger size Mg–Li–Sn rich precipitate affects the stress distribution and act as stress concentrator while the finer Mg–Al–Li rich precipitate effectively transfer the load to the β-phase and behave as stress relaxer. The α-phase is stiffer and harder while the β-phase is softer, which contribute in the release of the stress of matrix (Figs. 3 and 4). In our earlier publication, dislocation density of α- and β-phases were calculated by well-established statistical models [20]. The results of dislocation density calculation from Morris' model demonstrated the difference of an order of magnitude in dislocation density in both alloys, LAT971R and LATZ9531R (10^9 cm^{-2} for α-phase and 10^8 cm^{-2} for β-phase) [20]. Authors have also demonstrated the correlation between dislocation density and pop-in behavior. Large number of pop-in events were witnessed in α-phase (16–22 out of 25) compared to β-phase (10–15 out of 25) [20]. These factors all together are held responsible for stress concentration in matrix α-phase in contrast to that of reinforcing β-phase.
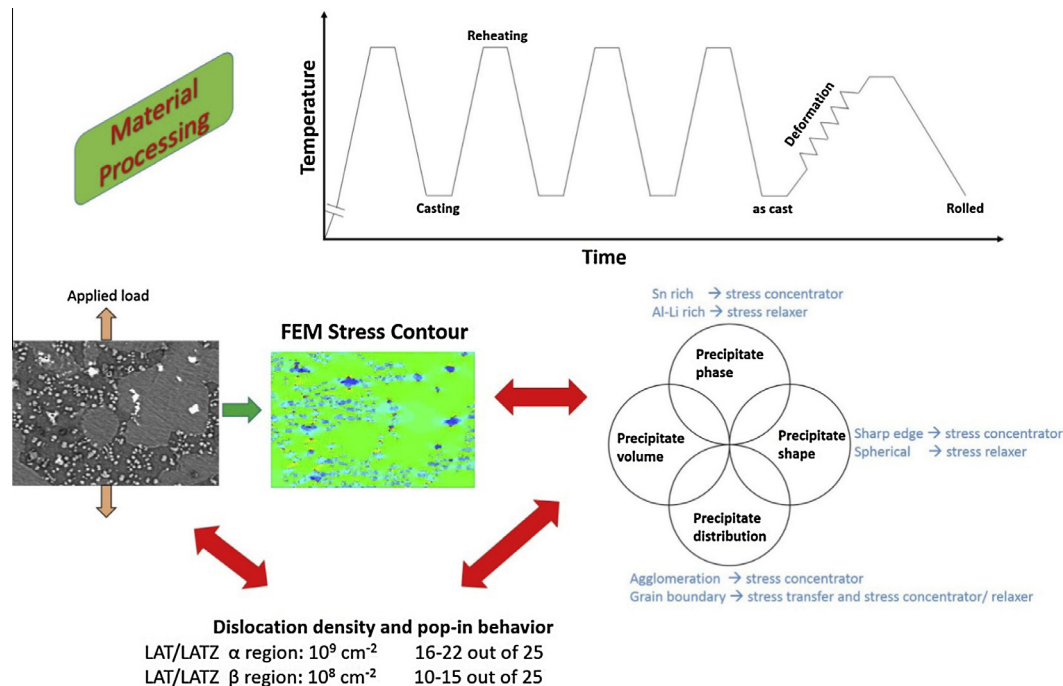
Fig. 4. Schematic showing the material processing of Mg-based alloys and demonstrating various parameters affect the stress distribution in the processed alloy.

Thus, the combination of nanoindentation and FEM stress analysis provide a quick and versatile method to predict the performance of material under various service conditions. Additionally, this combination also provides the opportunity to bridge the gap between nano and micro length scale mechanical properties and render better understanding of the stress concentrations being generated at specific microstructural features in dictating material's response to imposed engineering strains.

4. Conclusions

The mechanical behavior of the magnesium–lithium (Mg–Li) based novel LAT971 and LATZ9531 alloys in cast and rolled conditions have been studied using object oriented finite element modeling (OOFEM) based modeling tool and micromechanics models i.e. rule of mixture, combined Voigt–Reuss, Cox, Guth and Halpin–Tsai methods.

The effective elastic modulus values 50.7–56.3 GPa and 52.4–57.5 GPa have been estimated from theoretical models of Halpin–Tsai and combined Voigt–Reuss method, respectively. The predicted modulus values from Halpin–Tsai and combined Voigt–Reuss method shows close proximity and consistency compared to other micromechanics models (46.4–58.1 GPa for rule of mixture, 39.0–42 GPa for Cox method and 127.1–384.5 GPa for Guth model). This large deviation in the estimated modulus values have been attributed to reliance of various models on parameters such as volume fraction of second phase, particle shape and their agglomeration tendency. LATZ9531 alloy have shown slightly higher stress level (1.91 GPa) than LAT971 alloy (1.78 GPa) in as cast condition due to the change in the relative fraction of precipitate phase and change in chemical composition. Thermomechanical processing of Mg–Li alloys increase the stress level by 0.4 GPa for LAT971 and 1.13 GPa for LATZ9531 alloy. Effective elastic modulus of 55–60 GPa estimated using FEM is in good agreement with Halpin–Tsai and combined Voigt–Reuss micromechanics models. Moreover, Mg–Li alloys show heterogeneous local stress distribution in both, tensile and compression state where Mg–Al–Li rich precipitates act as stress relaxers in the β phase. On the other hand, most of the stress concentration was observed in the regions around Mg–Li–Sn rich precipitates in the α phase leading to the possibility of crack initiation and propagation. Nanoindentation study of α-, β- and precipitates phases disclose the mismatch in the elastic modulus which originate the heterogeneous stresses throughout the microstructure of Mg–Li alloys. Therefore, OOFEM has the potential in analyzing/accounting multi length scale effects using nanoindentation, microstructural incorporation of phase-distribution and their content and applying potential service conditions.

Appendix A. Supplementary material

Supplementary data associated with this article can be found, in the online version, at http://dx.doi.org/10.1016/j.jallcom.2015.02.066.

References

[1] F. Cardarelli, Materials Handbook: A Consise Desktop Reference, second ed., Springer, London, 2008.
[2] L. Wu, C. Cui, R. Wu, J. Li, H. Zhan, M. Zhang, Effects of Ce-rich RE additions and heat treatment on the microstructure and tensile properties of Mg–Li–Al–Zn-based alloy, Mater. Sci. Eng. A 528 (2011) 2174–2179.
[3] ASM Handbook: Properties and Selection: Nonferrous Alloys and Special-Purpose Materials, second ed., ASM International, Materials Park, 1992.
[4] R. Schmid-Fetzer, J. Gröbner, Thermodynamic database for Mg alloys – progress in multicomponent modeling, Metals 2 (2012) 377–398.

[5] G.S. Song, M. Staiger, M. Kral, Enhancement of the properties of Mg–Li alloys by small alloying addition, in: H.I. Kaplan (Ed.), Magnesium Technology 2003, Wiley, San Diego, 2003, pp. 77–79.

[6] T.-C. Chang, J.-Y. Wang, C.-L. Chu, S. Lee, Mechanical properties and microstructures of various Mg–Li alloys, Mater. Lett. 60 (2006) 3272–3276.

[7] B.A. Shaw, Corrosion resistance of magnesium alloys, in: S.D. Cramer, J. Bernard, S. Covino (Eds.), Corrosion: Fundamentals, Testing, and Protection, ASM International, Materials Park, 2003, pp. 692–696.

[8] I.J. Polmear, Recent developments in light alloys, Mater. Trans., JIM 37 (1996) 12–31.

[9] S. Kamado, Y. Kojima, Deformation and strengthening of superlight Mg–Li alloys, Metall. Sci. Technol. 16 (1998) 45–54.

[10] V. Kumar, Microstructural, Mechanical and Electrochemical Characterization of Thermomechanically Processed Mg–Li–Al Based Alloys, Indian Institute of Technology Kanpur, Kanpur, 2012.

[11] V. Kumar, Govind, R. Shekhar, R. Balasubramaniam, K. Balani, Microstructure evolution and texture development in thermomechanically processed Mg–Li–Al based alloys, Mater. Sci. Eng. A 547 (2012) 38–50.

[12] A. Agarwal, S.R. Bakshi, D. Lahiri, Carbon Nanotubes Reinforced Metal Matrix Composites, CRC Press, New York, 2011.

[13] S.R. Bakshi, A. Bhargava, S. Mohammadizadeh, A. Agarwal, I. Tsukanov, Computational estimation of elastic properties of spark plasma sintered TaC by meshfree and finite element methods, Comput. Mater. Sci. 50 (2011) 2615–2620.

[14] T. Mori, K. Tanaka, Average stress in matrix and average elastic energy of materials with misfitting inclusions, Acta Metall. Mater. 21 (1973) 571–574.

[15] Z. Hashin, S. Shtrikman, A variational approach to the theory of the elastic behavior of multiphase materials, J. Mech. Phys. Solids 11 (1963) 127–140.

[16] S.A. Langer, J.E.R. Fuller, W.C. Carter, OOF: an image-based finite-element analysis of material microstructures, Comput. Sci. Eng. 3 (2001) 15–23.

[17] K. Balani, R.R. Patel, A.K. Keshri, D. Lahiri, A. Agarwal, Multi-scale hierarchy of Chelydra serpentina: microstructure and mechanical properties of turtle shell, J. Mech. Behav. Biomed. 4 (2011) 1440–1451.

[18] S.R. Bakshi, R.R. Patel, A. Agarwal, Thermal conductivity of carbon nanotube reinforced aluminum composites: a multi-scale study using object oriented finite element method, Comput. Mater. Sci. 50 (2010) 419–428.

[19] N.K. Sharma, S.N. Pandit, R. Vaish, V. Srivastava, Effective Young's modulus of Ni–Al_2O_3 composites with particulate and interpenetrating phase structures: a multiscale analysis using object oriented finite element method, Comput. Mater. Sci. 82 (2014) 320–324.

[20] V. Kumar, A. Gupta, D. Lahiri, K. Balani, Serrated yielding during nanoindentation of thermomechanically processed novel Mg–9Li–7Al–1Sn and Mg–9Li–5Al–3Sn–1Zn alloys, J. Phys. D: Appl. Phys. 46 (2013) 145304–145308.

[21] W.C. Oliver, G.M. Pharr, An improved technique for determining hardness and elastic modulus using load and displacement sensing indentation experiments, J. Mater. Res. 7 (1992) 1564–1583.

[22] A.C.E. Reid, S.A. Langer, R.C. Lua, V.R. Coffman, S.-I. Haan, R.E. García, Image-based finite element mesh construction for material microstructures, Comput. Mater. Sci. 43 (2008) 989–999.

[23] A.C.E. Reid, R.C. Lua, R.E. García, V.R. Coffman, S.A. Langer, Modelling microstructures with OOF2, Int. J. Mater. Prod. Technol. 35 (2009) 361–373.

[24] S.R. Bakshi, D. Lahiri, A. Agarwal, Carbon nanotube reinforced metal matrix composites – a review, Int. Mater. Rev. 55 (2010) 41–64.

[25] T. Laha, A. Agarwal, N.B. Dahotre, The effective elastic modulus of laser-engineered composites boride coatings, Adv. Eng. Mater. 7 (2005) 626–629.

[26] A. Gupta, S. Sharma, M.R. Joshi, P. Agarwal, K. Balani, Grain growth behavior of Al_2O_3 nanomaterials: a review, Mater. Sci. Forum 653 (2010) 87–130.

[27] S. Ariharan, A. Gupta, A. Keshri, A. Agarwal, K. Balani, Size effect of yttria stabilized zirconia addition on fracture toughness and thermal conductivity of plasma sprayed aluminum oxide composite coatings, Nanosci. Nanotechnol. Lett. 4 (2012) 323–332.

[28] E. Guth, Theory of filler reinforcement, J. Appl. Phys. 16 (1945) 20–25.

[29] W. Yan, R.J.T. Lin, D. Bhattacharyya, Particulate reinforced rotationally moulded polyethylene composites – mixing methods and mechanical properties, Compos. Sci. Technol. 66 (2006) 2080–2088.

[30] K.J. Ganesh, S. Rajasekhara, J.P. Zhou, P.J. Ferreira, Texture and stress analysis of 120 nm copper interconnects, Scr. Mater. 62 (2010) 843–846.

[31] S.A. Asgari, P.D. Hodgson, C. Yang, B.F. Rolfe, Modeling of advanced high strength steels with the realistic microstructure–strength relationships, Compos. Mater. Sci. 45 (2009) 860–866.